Substitution of Bi for Sb and its Role in the Thermoelectric Properties and Nanostructuring in $Ag_{1-x}Pb_{18}MTe_{20}$ (M = Bi, Sb) (x = 0, 0.14, 0.3)

Mi-Kyung Han,[†] Khang Hoang,[‡] Huijun Kong,[§] Robert Pcionek,[||] Ctirad Uher,[§] Konstantinos M. Paraskevopoulos,[⊥] S. D. Mahanti,[‡] and Mercouri G. Kanatzidis*[,†]

Department of Chemistry, Northwestern University, Evanston, Illinois 60208, Department of Physics and Astronomy, Michigan State University, East Lansing, Michigan 48824, Department of Physics, University of Michigan, Ann Arbor, Michigan 48109, Department of Chemistry, Michigan State University, East Lansing, Michigan 48824, and Solid State Physics Section, Physics Department, Aristotle University of Thessaloniki, 54124 Thessaloniki, Greece

Received December 21, 2007. Revised Manuscript Received February 5, 2008

We have performed a comparative investigation of the $Ag_{1-x}Pb_{18}MTe_{20}$ (M = Bi, Sb) (x = 0, 0.14, 0.3) system to assess the roles of Sb and Bi on the thermoelectric properties. Detailed charge transport data including electrical conductivity, the Seebeck coefficient, the Hall coefficient, and thermal conductivity are presented. Optical reflectivity data support the conclusions of the transport studies. For comparable nominal compositions, the carrier concentrations are lower in the Sb analogs and the mobilities are higher. The Seebeck coefficient decreases dramatically in going from Sb to Bi. High resolution transmission electron microscopy (TEM) images of both samples reveal that all systems contain compositional fluctuations at the nanoscopic level and are nanostructured. Compared to PbTe, the lattice thermal conductivity of $AgPb_{18}BiTe_{20}$ is substantially reduced. The lattice thermal conductivity of the Bi analog is, however, higher than the Sb analog, and this correlates with the decrease in the degree of mass fluctuation between the nanostructures and the matrix (for the Bi analog). As a result the dimensionless figure of merit ZT of $Ag_{1-x}Pb_{18}BiTe_{20}$ is found to be substantially smaller than that of $Ag_{1-x}Pb_{18}SbTe_{20}$. Electronic structure calculations performed within the density functional theory and generalized gradient approximation show marked differences in the band structure near the Fermi level between the two analogs providing useful insights on the carrier transport in these systems.

Introduction

Thermoelectricity is based on the Peltier−Seebeck effect, which is the direct conversion between thermal and electrical energy, and can be used for heating and cooling applications.[1,2] The performance of a thermoelectric material is assessed with the figure of merit ZT defined as $(S^2\sigma/\kappa)T$; where S is the Seebeck coefficient (or thermopower), σ is the electrical conductivity, κ is the thermal conductivity, and T is the temperature. High performance thermoelectric materials require a large Seebeck coefficient and electrical conductivity and low thermal conductivity. The main challenge in enhancing ZT lies in the interdependence of the physical parameters that define ZT.[3,4] Typically, degenerate semiconductors with optimized mobility and carrier concentration are the focus since the underlying physics of these systems allow the coexistence of high Seebeck coefficient values with high electrical conductivity. A variety of materials in the form of thin film[5–8] or bulk samples[9–22] have been studied with respect to their thermoelectric properties and significant

* To whom correspondence should be addressed. E-mail: m-kanatzidis@northwestern.edu.
[†] Northwestern University.
[‡] Department of Physics and Astronomy, Michigan State University.
[§] Department of Physics, University of Michigan.
[||] Department of Chemistry, Michigan State University.
[⊥] Aristotle University of Thessaloniki.

(1) Wood, C. *Rep. Prog. Phys.* **1988**, *51*, 459–539.
(2) Rowe, D. M. *CRC Handbook of Thermoelectrics*; CRC Press: New York, 1995.
(3) Nolas, G. S.; Poon, J.; Kanatzidis, M. *MRS Bull.* **2006**, *31* (3), 199.
(4) Kanatzidis, M. G. The role of solid-state chemistry in the discovery of new thermoelectric materials. In *Recent Trends in Thermoelectric Materials Research I*; 2001; Vol. 69, p 51.
(5) Harman, T. C.; Taylor, P. J.; Walsh, M. P.; LaForge, B. E. *Science* **2002**, *297*, 2229.
(6) Harman, T. C.; Walsh, M. P.; LaForge, B. E.; Turner, G. W. *J. Electron. Mater.* **2005**, *34*, L19.
(7) Dresselhaus, M. S.; Chen, G.; Tang, M. Y.; Yang, R.; Lee, H.; Wang, D.; Ren, Z.; Fleurial, J.; Gogna, P. *Adv. Mater.* **2007**, *19*, 1.
(8) Venkatasubramanian, R.; Siivola, E.; Colpitts, T.; O'Quinn, B. *Nature* **2001**, *413*, 597.
(9) Hsu, K. F.; Loo, S.; Guo, F.; Chen, W.; Dyck, J. S.; Uher, C.; Hogan, T.; Polychroniadis, E. K.; Kanatzidis, M. G. *Science* **2004**, *303*, 818.
(10) Quarez, E.; Hsu, K. F.; Pcionek, R.; Frangis, N.; Polychroniadis, E. K.; Kanatzidis, M. G. *J. Am. Chem. Soc.* **2005**, *127*, 9177.
(11) Poudeu, P. F. P.; D'Angelo, J.; Downey, A. D.; Short, J. L.; Hogan, T. P.; Kanatzidis, M. G. *Angew. Chem., Int. Ed.* **2006**, *45*, 3835.
(12) Androulakis, J.; Pcionek, R.; Quarez, E.; Do, J.-H.; Kong, H.; Palchik, O.; Uher, C.; Hogan, T. P.; Kanatzidis, M. G. *Chem. Mater.* **2006**, *18*, 4719.
(13) Lee, K. H.; Kim, S. W.; Ohta, H.; Koumoto, K. *J. Appl. Phys.* **2007**, *101* (8), 083707.
(14) Wilson-Short, G. B.; Singh, D. J.; Fornari, M.; Suewattana, M. *Phys. Rev. B: Condens. Matter Mater. Phys.* **2007**, *75* (3), 035121.
(15) Condron, C. L.; Kauzlarich, S. M.; Nolas, G. S. *Inorg. Chem.* **2007**, *46* (7), 2556.
(16) Kyratsi, T.; Hatzikraniotis, E.; Paraskevopoulos, K. M.; Malliakas, C. D.; Dyck, J. S.; Uher, C.; Kanatzidis, M. G. *J. Appl. Phys.* **2006**, *100* (12), 123704.
(17) Kyratsi, T.; Dyck, J. S.; Chen, W.; Chung, D. Y.; Uher, C.; Paraskevopoulos, K. M.; Kanatzidis, M. G. *J. Appl. Phys.* **2002**, *92* (2), 965.

10.1021/cm703661g CCC: $40.75
Published on Web 04/25/2008

progress has been achieved in raising ZT. On the basis of theoretical[23–26] and experimental works, attempts to achieve enhanced ZT have involved (a) choosing the appropriate combination of different metals and nonmetals to have desired crystal structures and carrier doping and (b) constructing nanostructured materials to have sharper density of states (DOS) near the Fermi level to enhance *S* and increase phonon scattering from embedded nanostructures.

Recently, we reported that the $Ag_{1-x}Pb_{18}SbTe_{20}$ system can achieve an impressively high figure of merit.[9] Such improvement represented an approximately 100% enhancement of the ZT of optimized PbTe itself, and was achieved by a greatly reduced lattice thermal conductivity caused by embedded nanostructured precipitates in the bulk system. Electron microscopy studies of $Ag_{1-x}Pb_{18}SbTe_{20}$ confirmed the existence of nanodots rich in Ag−Sb embedded endotaxially in a PbTe matrix.[25,27] Subsequently, we reported other similar quaternary systems with ZT > 1.5.[11,28–30] Based on ab initio electronic structure calculations, Bilc et al. suggested that significant changes in the electronic DOS near the band gap region could result from microstructural arrangements of Ag−Sb atoms in PbTe lattice.[25] These developments have led to a better fundamental understanding of the substitution effects of different elements in the PbTe lattice on different physical properties, nanoscale structures, and electronic structure in this system.

In this work, we have investigated the role of the two trivalent elements Sb and Bi in the nanostructuring, electronic structure, as well as thermoelectric properties by conducting comparative studies of Sb and Bi analogs. Namely, the series of $Ag_{1-x}Pb_{18}BiTe_{20}$ ($x = 0, 0.14, 0.3$) samples was investigated and compared with a corresponding series of $Ag_{1-x}Pb_{18}SbTe_{20}$ ($x = 0, 0.14, 0.3$) (LAST-18) compositions prepared under similar conditions. We show that $Ag_{1-x}Pb_{18}BiTe_{20}$ (BLST-18) is also nanostructured like LAST, and the nature of the trivalent element is in fact critical in controlling the charge and thermal transport properties. Our work shows that, for the same composition, Sb is superior to Bi in giving larger power factor and lower lattice thermal conductivity and, therefore, seems to be responsible for the enhanced thermoelectric properties of the LAST system.

Experimental Section

Synthesis. Ingots (~10 g) with nominal compositions of $AgPb_{18}SbTe_{20}$, $Ag_{0.86}Pb_{18}SbTe_{20}$, $Ag_{0.7}Pb_{18}SbTe_{20}$, $AgPb_{18}BiTe_{20}$, $Ag_{0.86}Pb_{18}BiTe_{20}$, and $Ag_{0.7}Pb_{18}BiTe_{20}$ were synthesized by mixing appropriate stoichiometric ratios of high purity starting elemental materials, namely Ag, Pb, Sb, Bi, and Te (>99.99% in purity). The corresponding elements were sealed in appropriate ratio in evacuated fused silica tubes (10 mm diameter, 1 mm wall thickness) under a residual pressure of $\sim 10^{-4}$ Torr. The sealed tubes were heated to 1050 °C over 24 h and then held there for 24 h while rocking the liquid to facilitate complete mixing of the contents. The final step consisted of two parts: (1) slow cooling to 700 °C at a rate of 2 °C/h and (2) rapid cooling from 700 °C to room temperature over 12 h. Single dense ingots were obtained with a dark silvery metallic shine. The ingots are stable in water and air and are relatively brittle.

Powder X-ray Diffraction. The powder diffraction patterns were obtained with an Inel diffractometer equipped with a position sensitive detector and operating at 40 kV and 20 mA. Data acquisition was controlled via the *In-Situ* program. The lattice parameters of $Ag_{1-x}Pb_{18}MTe_{20}$ (M = Bi, Sb) were obtained from least-squares refinement of data in the range of 2θ between 10° and 80° with the aid of a *Rietveld* refinement program. X-ray powder diffraction patterns showed single phase products crystallizing in a cubic fcc lattice (NaCl-type).

Differential Thermal Analysis (DTA). DTA analyses were performed with a Shimadzu DTA-50 thermal analyzer. Approximately 30 mg of ground powder was sealed in a quartz ampule under vacuum ($\sim 10^{-4}$ Torr). A silica ampule containing equivalent mass of alumina (Al_2O_3) sealed in same ampule was used as a reference. The samples were heated to 1000 °C at a rate of 10 °C/min, isothermed for 3 min, and then cooled to 200 °C at a rate of 10 °C/min. The temperature difference between the sample and the reference was monitored during two heating and cooling cycles.

Thermal Conductivity. The thermal conductivity (κ_{tot}) can be derived from the relationship $\kappa_{tot}(T) = D(T)C_p(T)\rho(T)$, where C_p is the specific heat, $D(T)$ is the thermal diffusivity, and $\rho(T)$ is the density of the sample.

Specific heat (C_p) and thermal diffusivity (D) of several specimens were determined by the flash diffusivity-heat capacity method using NETZSCH LFA 457 MicroFlash instrument. In the flash diffusivity method, the front face of a disk-shaped plane-parallel (8 mm or 13 mm diameter; 1−2 mm thickness) is heated by a short energy pulse, e.g. a laser beam. The thermal diffusivity is determined by the shape of the temperature rise on the rear sample surface versus time using an infrared detector. Density ($\rho(T)$) was calculated from the sample's geometry and mass.

Electrical Properties. The samples were cut to rectangular shape of about $3 \times 3 \times 8$ mm^3 for measurement of electrical properties. The longer direction coincides with the direction in which the thermal conductivity is measured. Electrical conductivity and Seebeck coefficient were measured simultaneously under a helium atmosphere from room temperature to about 650 K using a ULVAC-RIKO ZEM-3 instrument system. Electrical conductivity was measured with the 4-probe method and the Seebeck coefficient

(18) Chung, D. Y.; Hogan, T.; Brazis, P.; Rocci-Lane, M.; Kannewurf, C.; Bastea, M.; Uher, C.; Kanatzidis, M. G. *Science* **2000**, *287* (5455), 1024.
(19) Chung, D. Y.; Choi, K. S.; Iordanidis, L.; Schindler, J. L.; Brazis, P. W.; Kannewurf, C. R.; Chen, B. X.; Hu, S. Q.; Uher, C.; Kanatzidis, M. G. *Chem. Mater.* **1997**, *9* (12), 3060.
(20) Kanatzidis, M. G.; McCarthy, T. J.; Tanzer, T. A.; Chen, L. H.; Iordanidis, L.; Hogan, T.; Kannewurf, C. R.; Uher, C.; Chen, B. X. *Chem. Mater.* **1996**, *8* (7), 1465.
(21) Tang, X. F.; Zhang, Q. J.; Chen, L. D.; Goto, T.; Hirai, T. *J. Appl. Phys.* **2005**, *97* (9), 093712.
(22) Tang, X. F.; Zhang, L. M.; Yuan, R. Z.; Chen, L. D.; Goto, T.; Hirai, T.; Dyck, J. S.; Chen, W.; Uher, C. *J. Mater. Res.* **2001**, *16* (12), 3343.
(23) Ahmad, S.; Mahanti, S. D.; Hoang, K.; Kanatzidis, M. G. *Phys. Rev. B* **2006**, *74*, 155205.
(24) Hazama, H.; Mizutani, U.; Asahi, R. *Phys. Rev. B* **2006**, *73*, 115108.
(25) Bilc, D.; Mahanti, S. D.; Quarez, E.; Hsu, K. F.; Pcionek, R.; Kanatzidis, M. G. *Phys. Rev. Lett.* **2004**, *93*, 146403.
(26) Ahmad, S.; Hoang, K.; Mahanti, S. D. *Phys. Rev. Lett.* **2006**, *96*, 056403.
(27) Heremans, J. P.; Thrush, C. M.; Morelli, D. T. *Phys. Rev. B* **2004**, *70*, 225334.
(28) Androulakis, J.; Hsu, K. F.; Pcionek, R.; Kong, H.; Uher, C.; DÁngelo, J.; Downey, A. D.; Hogan, T. P.; Kanatzidis, M. G. *Adv. Mater.* **2006**, *18*, 1170.
(29) Androulakis, J.; Lin, C. H.; Kong, H. J.; Uher, C.; Wu, C. I.; Hogan, T.; Cook, B. A.; Caillat, T.; Paraskevopoulos, K. M.; Kanatzidis, M. G. *J. Am. Chem. Soc.* **2007**, *129* (31), 9780–9788.
(30) Poudeu, P. F. P.; DÁngelo, J.; Kong, H.; Downey, A. D.; Short, J. L.; Pcionek, R.; Hogan, T. P.; Uher, C.; Kanatzidis, M. G. *J. Am. Chem. Soc.* **2006**, *126*, 14347.

was measured three times with different temperature gradients from 5 to 15 K at each temperature step.

Infrared Spectroscopy. To probe the optical energy band gap of the series, room temperature optical diffuse reflectance measurements were performed using a Nicolet 6700 FTIR spectrometer. The spectra were monitored in the mid-IR region (6000–400 cm^{-1}). Absorption data were calculated from reflectance data using the Kubelka–Munk function. The optical band gaps were derived from absorption versus E (eV) plots.[31–33] Specular IR reflectivity measurements were carried out on polished specimens in the spectral range 100 –2500 cm^{-1}, at room temperature, with nonpolarized light, using a Bruker IFS 113v Fourier transform interferometer working under vacuum and equipped with the special reflectance unit. The angle of incidence was less than 10°.

High-Resolution Transmission Electron Microscopy. The microstructures of samples were examined using high-resolution transmission electron microscopy (HRTEM). HRTEM images of several pieces cut from different locations of the ingots were obtained at 200 kV using a JEOL JEM 2200FS (Filed emission TEM). Samples of $Ag_{1-x}Pb_{18}MTe_{20}$ (M = Bi, Sb) were prepared for examination in the TEM by the conventional methods of lapping, dimple grinding, and ion mill polishing. A typical sample consisted of a slab mounted on a copper aperture grid having a total rim thickness of around 130 μm and dimpled to a depth of about 45 μm on the top side (and in some cases a shallow dimple on the bottom side). Ion mill polishing to electron transparency was achieved with a Gatan Model 691 precision ion polishing system (PIPS) operated at initial beam energies of 3.2 or 3.1 keV. Specimens were mounted in the PIPS using the clamp-type DuoPost.

Hall Measurements. The Hall voltage was measured using a Quantum Design MPMS (magnetic property measurement system) and a Linear Research AC bridge with 16 Hz excitation. Within the MPMS Dewar, a cryogenic probe integrates a five Tesla superconducting magnet with four-probe AC Hall measurements over a temperature range of 1.9−300 K. Four-wire AC Hall measurements were performed on parallelepiped samples with the typical size of $1 \times 3 \times 5$ mm^3. The current and Hall voltage leads were fine copper wires, and the contacts were made of indium solder.

Electronic Structure Calculation. In order to understand the difference between Sb and Bi analogs, ab initio electronic structure calculations were carried out using density functional theory (DFT). The effect of replacing Pb by (Ag, Sb) or (Ag, Bi) on the electronic structures was investigated using a supercell model. In this model, Ag, Sb, and Bi were assumed to substitute for some of the Pb atoms of the host material PbTe. In our calculation we took two substitutional atoms (Ag, Sb) or (Ag, Bi) replacing two Pb atoms in a 64-atom supercell. This corresponds to the formula $AgPb_mMTe_{m+2}$ (m = 30; M = Sb, Bi). In the supercell model, the substitutional atoms are periodically arranged in the host PbTe crystal. Structural optimization, total energy and electronic structure calculations were performed using the generalized-gradient approximation (GGA)[34] and the projector-augmented wave (PAW)[35,36] method as implemented in Vienna ab initio simulation package (VASP).[37–39] We treated the outermost s and p electrons of Pb, Te, and the impurities, as valence electrons and the rest as cores; scalar relativistic effects

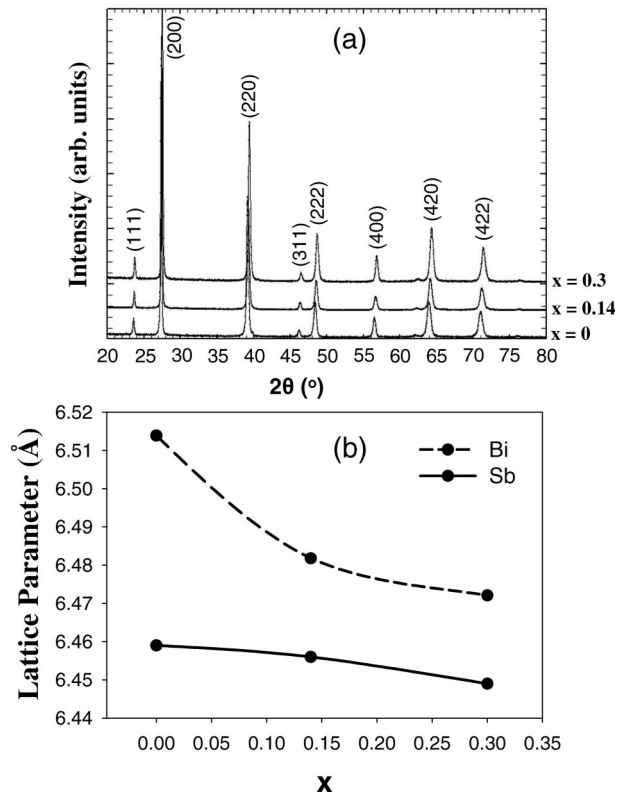

Figure 1. (a) Powder X-ray diffraction patterns of $Ag_{1-x}Pb_{18}SbTe_{20}$ (x = 0, 0.14, 0.3) samples. (b) Variation of unit cell parameter as a function of x for the $Ag_{1-x}Pb_{18}MTe_{20}$ (M = Bi, Sb) (x = 0, 0.14, 0.3) samples.

(mass-velocity and Darwin terms) and spin–orbit interaction (SOI) were included. The energy cutoff was set up to 300 eV, and the convergence was assumed when the total energy difference between consecutive cycles was within 10^{-4} eV. Structural optimization was carried out without SOI since it was found that the inclusion of SOI did not have significant influence on the structural properties. The optimized lattice constant of pure PbTe (a = 6.55 Å) was used to set up the initial structures. All atomic coordinates were then relaxed using the conjugate-gradient algorithm with a tolerance factor of 10^{-3} eV/Å for the force minimization. Each defect calculation began with ionic optimization; the relaxed supercell was then used to calculate energy and the band structure.

Results and Discussion

Since the electrical transport properties of $Ag_{1-x}Pb_{18}MTe_{20}$ (M = Bi, Sb) (x = 0, 0.14, 0.3) are very sensitive to the preparation conditions, all samples were prepared with identical experimental conditions for meaningful comparison. The X-ray diffraction (XRD) pattern and unit cell parameter variation as a function of x for the $Ag_{1-x}Pb_{18}MTe_{20}$ (M = Bi, Sb) (x = 0, 0.14, 0.3) samples are shown in Figure 1. The XRD patterns show single phases crystallizing in a cubic NaCl-type structure with the space group of $Fm\bar{3}m$. As shown in Figure 1b, the substitution of Sb atoms (atomic radius ~1.45 Å) with bigger Bi atoms (radius ~1.60 Å) leads to an increase of the lattice parameter. The lattice parameters decrease with decreasing Ag content in both series of samples, but decreases much more rapidly for the Bi analog. It is not clear at this stage how the deficiency of Ag is accommodated in the $Ag_{1-x}Pb_{18}MTe_{20}$ structure. One possibility is for the deficiency to manifest itself as vacancies

(31) Wendlandt, W. W.; Hecht, H. G. Interscience Publishers: New York, 1966.
(32) Kotuem, G. Springer-Verlag: New York, 1969.
(33) Tandon, S. P.; Gupta, J. P. *Status Solidi* **1970**, *38*, 363.
(34) Perdew, J. P.; Burke, K.; Ernzerhof, M. *Phys. Rev. Lett.* **1996**, *77*, 3865.
(35) Blöchl, P. E. *Phys. Rev. B* **1994**, *50*, 17953.
(36) Kresse, G.; Joubert, D. *Phys. Rev. B* **1999**, *59*, 1758.
(37) Kresse, G.; Hafner, J. *Phys. Rev. B* **1993**, *47*, 558.
(38) Kresse, G.; Hafner, J. *Phys. Rev. B* **1994**, *49*, 14251.
(39) Kresse, G.; Furthmüller, J. *Phys. Rev. B* **1996**, *54*, 11169.

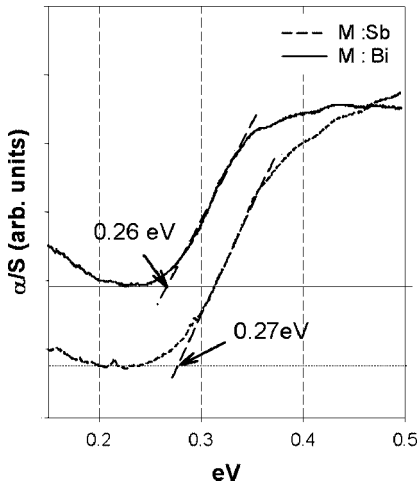

Figure 2. Infrared absorption spectra and energy band gap of $Ag_{1-x}Pb_{18}MTe_{20}$ (M = Sb, Bi) ($x = 0.14$).

at the Na sites of the NaCl lattice. This is unlikely since it will create p-type samples which is not observed. Another is that vacancies are not formed keeping the Ag to M ratio 1:1. In this case a small fraction of Sb or Bi (equal to the value of x) become excess, some of the excess Sb or Bi could serve as an *n*-type dopant while the rest could be expelled from the lattice as a minor phase. Investigations along these lines are underway.

Figure 2 shows a typical infrared absorption spectrum for samples of $AgPb_{18}MTe_{20}$ (M = Bi, Sb). All members of the series are narrow gap semiconductors with spectroscopically observable energy bandgaps in the infrared region between 0.26 and 0.28 eV. These band gaps are very close to that of PbTe itself.[1]

Differential thermal analysis of $Ag_{1-x}Pb_{18}MTe_{20}$ (M = Bi, Sb) samples show congruent melting with one endothermic melting peak during the heating cycle and one exothermic recrystallization peak during the cooling cycle. $AgPb_{18}BiTe_{20}$ melts at ~933 °C and crystallizes at ~914 °C, whereas $AgPb_{18}SbTe_{20}$ melts at ~925 °C and crystallizes at ~892 °C. The higher melting temperature of $Ag_{1-x}Pb_{18}BiTe_{20}$ can be attributed to the more ionic character of the Bi−Te vis-à-vis Sb−Te bond. With decreasing Ag content, the melting point of both series of $Ag_{1-x}Pb_{18}MTe_{20}$ (M = Sb, Bi) samples decreases slightly. The melting point for $Ag_{1-x}Pb_{18}BiTe_{20}$ ranges from 915 °C ($x = 0.3$) to 933 °C ($x = 0$), whereas for $Ag_{1-x}Pb_{18}SbTe_{20}$, it ranges from 920 °C ($x = 0.3$) to 925 °C ($x = 0$).

Charge Transport. Temperature dependence of the electrical conductivity σ of $Ag_{1-x}Pb_{18}MTe_{20}$ (M = Sb, Bi) is shown in Figure 3a and b. In both cases, σ decreases with increasing temperature T, consistent with previous results.[9] The decrease in σ is caused mainly by carrier phonon scattering. The temperature dependence follows a quadratic power law of $\sigma \sim T^{-2.12}$ and $\sigma \sim T^{-2.29}$ for $Ag_{0.86}Pb_{18}SbTe_{20}$ and $AgPb_{18}BiTe_{20}$, respectively, and it is similar to that observed for doped samples of PbTe where $\sigma \sim T^{-2.2}$.[28] The electrical conductivity of $Ag_{1-x}Pb_{18}SbTe_{20}$ samples increases with decreasing Ag content. The result for $AgPb_{18}SbTe_{20}$ shows relatively low electrical conductivity (~700 S/cm at room temperature). This can be caused by inhomogeneities

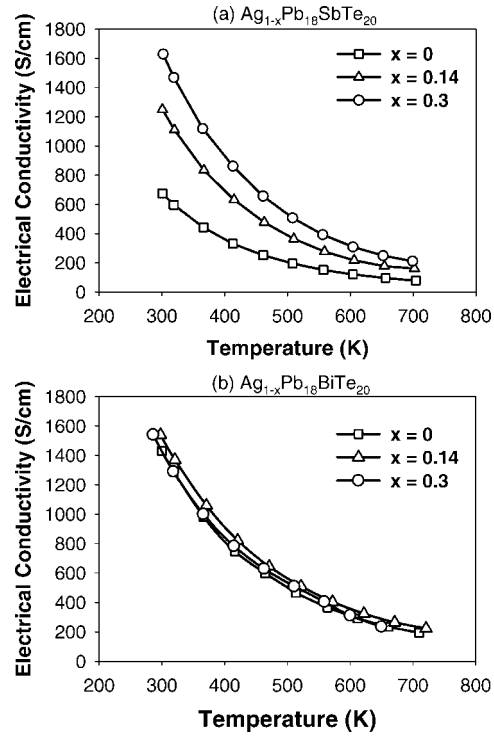

Figure 3. Temperature dependence of electrical conductivity of $Ag_{1-x}Pb_{18}MTe_{20}$ (M = Sb, Bi).

and microcracks but more likely it is due to lower doping levels since the members with other two x compositions showed much higher electrical conductivity in the range of 1200−1600 S/cm.[9] All three Bi samples showed large room temperature conductivities (~1500 S/cm).

Figure 4a and b present the temperature dependence of the Seebeck coefficient of $Ag_{1-x}Pb_{18}MTe_{20}$ (M = Sb, Bi). The Seebeck coefficient is negative in the whole temperature range, indicating that the majority of charge carriers are electrons (*n*-type). As the temperature increases, the Seebeck coefficient of $Ag_{1-x}Pb_{18}MTe_{20}$ (M = Sb, Bi) decrease more or less. The Seebeck coefficient for $Ag_{1-x}Pb_{18}SbTe_{20}$ ranges from approximately –100 μV/K at room temperature to approximately −350 μV/K at 700 K, whereas for $Ag_{1-x}Pb_{18}BiTe_{20}$, it ranges from approx −40 to approx −220 μV/K at 700 K. With increasing Ag contents, the magnitude of the Seebeck coefficient of both series $Ag_{1-x}Pb_{18}MTe_{20}$ (M = Sb, Bi) samples increases slightly. The changes are larger for the Sb analog.

The corresponding power factors ($S^2\sigma$) as a function of temperature T are given in Figure 5. For the $Ag_{1-x}Pb_{18}SbTe_{20}$ ($x = 0$, 0.14, 0.3) system, the power factor first increases with increasing T, reaches a maximum, and then decreases. For example, the $Ag_{1-x}Pb_{18}SbTe_{20}$ ($x = 0.14$) composition shows a maximum value of ~23.2 μW/cm·K^2 at 415 K. The power factor for $Ag_{1-x}Pb_{18}BiTe_{20}$ ($x = 0$, 0.14, 0.3) system also steadily increases with increasing T to 9.7 μW/cm·K^2 and then decreases slightly. The lower power factors of the $Ag_{1-x}Pb_{18}BiTe_{20}$ samples compared $Ag_{1-x}Pb_{18}SbTe_{20}$ arise from the smaller Seebeck coefficients. It is clear from these results that replacing Sb by Bi causes a significant decrease in the power factor without a significant change in the electrical conductivity. One reason for this could be a

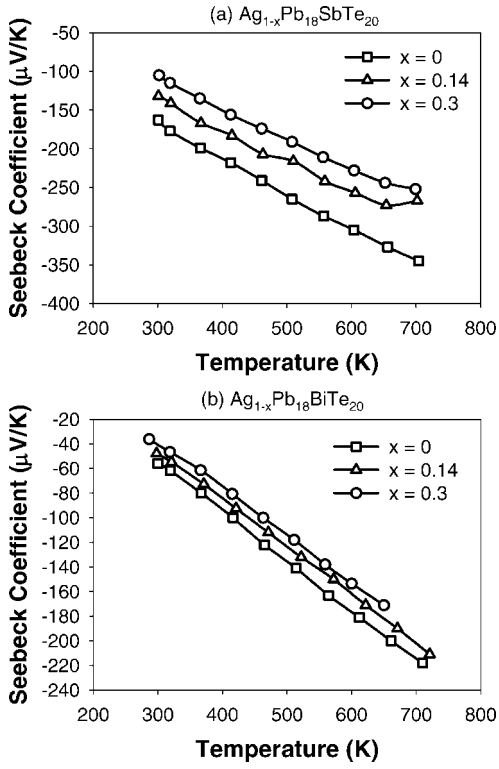

Figure 4. Temperature dependence of the Seebeck coefficient of $Ag_{1-x}Pb_{18}MTe_{20}$ (M = Sb, Bi).

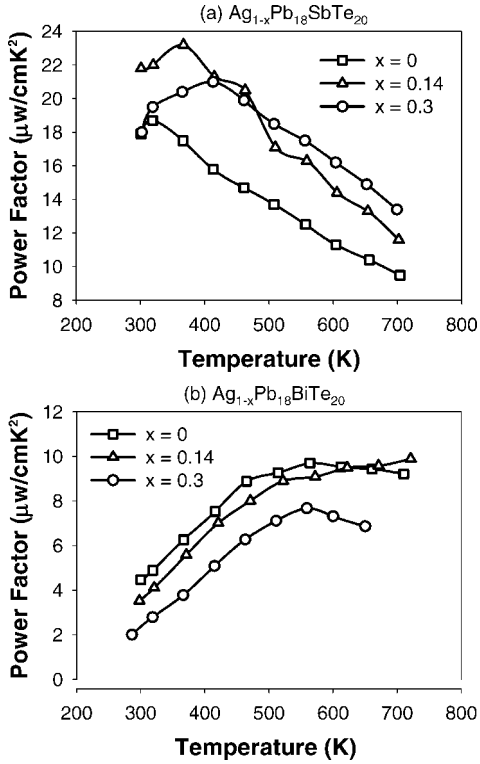

Figure 5. Temperature dependence of power factor of $Ag_{1-x}Pb_{18}MTe_{20}$ (M = Sb, Bi).

higher number of carriers in the Bi analogs. There could be other reasons involving changes in the electronic structure. To understand these transport properties, band structure calculations were carried out on these compounds and the results will be presented later in this paper.

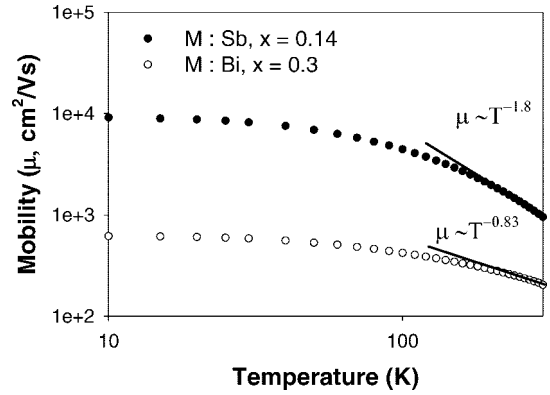

Figure 6. Variation of mobility with temperature in $Ag_{1-x}Pb_{18}MTe_{20}$ (M = Sb, Bi).

Table 1. Some Properties of $Ag_{1-x}Pb_{18}BiTe_{20}$ at 300 K, Compared with PbTe and $Ag_{1-x}Pb_{18}SbTe_{20}$

sample	type	carrier concentration (n) (10^{19} 1/cm^3)	mobility (cm^2/V•s)	ref
PbTe	n	0.5	$1-1.5 \times 10^3$	22
		$Ag_{1-x}Pb_{18}SbTe_{20}$		
$x = 0$	n	0.54	778	this work
$x = 0.14$	n	0.51	783	this work
$x = 0.33$	n	1.9	~800	7
		$Ag_{1-x}Pb_{18}BiTe_{20}$		
$x = 0$	n	4.19	192	this work
$x = 0.14$	n	3.04	222	this work
$x = 0.30$	n	5.04	178	this work

Hall measurements were carried out as a function of temperature. The Hall voltage was negative indicating n-type conduction, which is in agreement with the Seebeck coefficient measurements. Assuming one carrier type and a simple parabolic band model in our analysis, carrier concentration (n) was calculated from the room temperature Hall constants using the relationship $R_H = 1/ne$, where R_H is the Hall coefficient, n is the carrier concentration, and e is the electronic charge. Some physical properties of $Ag_{1-x}Pb_{18}BiTe_{20}$ in comparison with that of PbTe and $Ag_{1-x}Pb_{18}SbTe_{20}$ are listed in Table 1. The measured carrier concentration of $Ag_{1-x}Pb_{18}BiTe_{20}$ is of the order of approximately 10^{19} cm^{-3} which is much higher than that of $Ag_{1-x}Pb_{18}SbTe_{20}$ (see Table 1). Whether this discrepancy arises from the single band approximation will be discussed later. The large carrier concentration in $Ag_{1-x}Pb_{18}BiTe_{20}$ is consistent with the lower thermopower in these samples.

Figure 6 shows the variation of the Hall mobility with temperature on a logarithmic scale. The Hall mobility of both Sb and Bi systems decreases sharply above ~80 K. The power law dependence of $\mu \sim T^{-1.8}$ was observed in $Ag_{1-x}Pb_{18}SbTe_{20}$ ($x = 0.14$), in which acoustic phonon scattering is dominant near 300 K. In contrast, $Ag_{1-x}Pb_{18}BiTe_{20}$ ($x = 0.3$) has slower temperature variation $\mu \sim T^{-0.83}$. This low value for the exponent suggests that in addition to acoustic phonon scattering there are additional mechanisms, such as charged impurity scattering. One possible reason for the decrease in mobility of $Ag_{1-x}Pb_{18}BiTe_{20}$ system (other than the higher carrier concentration) may arise from stronger electron–phonon scattering. Because of the large difference in electronegativity

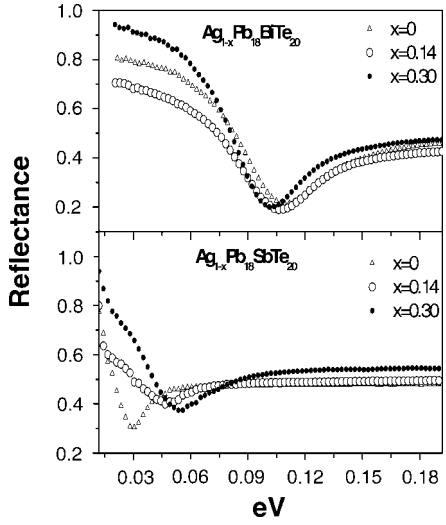

Figure 7. Specular reflectance spectra of $Ag_{1-x}Pb_{18}SbTe_{20}$ and $Ag_{1-x}Pb_{18}BiTe_{20}$ as a function of x. For the Bi analogs, the reflectivity minimum which is related to the plasma frequency ω_p lies at higher energies indicating a higher carrier concentration.

with Te (anionic sites), the bonding between Bi and Te has more ionic character, providing stronger scattering from phonons.

Optical Spectroscopy. Optical reflectance studies, interpreted within the framework of simple free electron models, can provide useful information on the electronic structure and transport characteristics of semiconductors. We used infrared reflectivity spectroscopy as a means for investigating the trends in carrier concentration and carrier effective mass as a function of trivalent element and Ag-deficiency in the title materials. However, we should be aware that the band structure of $Ag_{1-x}Pb_{18}BiTe_{20}$ may have significant deviation from a free electron single band model. The reflectivity spectra of the studied samples are shown in Figure 7. The minima of the reflectivity, $R(\omega)$, curves are sufficiently sharp to permit accurate determination of position using the numerical analysis procedures described in the experimental section. The LO-mode of the host lattice is influenced by the plasmon mode (ω_p) of the free carriers. As a result a combined plasmon-LO phonon mode should be observed. The numerical analysis of the experimental data was done using a form of the dielectric function that takes into account the existence of a plasmon-LO phonon interaction:

$$\varepsilon(\omega) = \varepsilon_\infty \frac{\prod_{j=1}^{2}(\omega^2 + i\gamma_{Lj}\omega - \omega_{Lj}^2)}{\omega(\omega + i\gamma_p)(\omega^2 + i\gamma_T\omega - \omega_T^2)} \prod_{n=1}^{p} \times \frac{(\omega^2 + i\gamma_{LOn}\omega - \omega_{LOn}^2)}{(\omega^2 + i\gamma_{TOn}\omega - \omega_{TOn}^2)} \prod_{k=1}^{3} \frac{(\omega^2 + i\gamma_{LOk}\omega - \omega_{LOk}^2)}{(\omega^2 + i\gamma_{TOk}\omega - \omega_{TOk}^2)} \quad (1)$$

Where, ω_{Lj} and γ_{Lj} parameters of the first numerator represent the eigen frequencies and the damping factors of the longitudinal plasmon−phonon waves (LP + LO), respectively; ω_T and γ_T are the frequency and damping factor of the transverse phonon mode; γ_p is the damping factor of plasmon, and ε_∞ is the high frequency dielectric permittivity. The second factor in eq 1 represents the Ag impurity local modes. The ω_{LOk} and ω_{TOk} are the longitudinal and transverse frequencies and γ_{LOk} and γ_{TOk} stand for the damping factors of uncoupled modes of the host crystal.

Table 2. Solid State Parameters of the $Ag_{1-x}Pb_{18}MTe_{20}$ Systems at 300 K, Obtained from Infrared Reflectivity Spectroscopy

	type	carrier concentration (10^{19} 1/cm^3)	ω_p (1/cm)	m^*/m_0
		$Ag_{1-x}Pb_{18}SbTe_{20}$		
$x = 0$	n	0.54	248	0.24
$x = 0.14$	n	0.51	391	0.08
$x = 0.30$	n	1.9	445	0.20
		$Ag_{1-x}Pb_{18}BiTe_{20}$		
$x = 0$	n	4.19	894	0.14
$x = 0.14$	n	3.04	873	0.12
$x = 0.30$	n	5.04	828	0.20

The plasma frequency is calculated from the relation

$$\omega_p = \frac{\omega_{L1}\omega_{L2}}{\omega_T} \quad (2)$$

From the formula relating the plasma frequency ω_p, the number of carriers N, electrons in our case, and the effective mass m^* we can calculate the effective mass, eq 3, $-e$ being the magnitude of the electron charge, ε_0 and ε_∞, the dielectric permittivity of vacuum and the high frequency range where the optical reflectivity was measured, respectively. The analysis results are given in Table 2.

$$\omega_p = \sqrt{\frac{Ne^2}{\varepsilon_0\varepsilon_\infty m^*}} \quad (3)$$

Looking at the spectra and the relative position of the plasma frequency ω_p, it can be concluded that generally the Sb analogs have much lower number of carriers compared to those with Bi. Regarding the Ag contribution, it is clear that the plasma frequency increases with increasing Ag content. This is in agreement with the transport results of the Hall effect experiments. While the spectra of the Bi analogs have a trend that varies with the gradually changing number of carriers changing with x, in the spectra of the Sb analogs, there is a more marked discrepancy. For example, for $x = 0$ the samples have an apparent lower number of defects and steeper rise of reflectivity edge, compared to those of $x = 0.14$ and $x = 0.30$ leading to greater charge carrier scattering and a more flat rising reflectivity at the plasma frequency.

Band Structure Calculations. To understand the fundamental differences in transport and spectroscopy observed for the Sb and Bi analogs, we examined the band structure near the band gap region. The results are quite revealing. To perform these calculations we took into account the following considerations. There are several ways of arranging the two substitutional atoms (Ag and M) on the metal (Pb) sites in a 64-atom supercell; they can be the first, the second, the third, the fourth, and the fifth nearest neighbors of one another (on the cation sublattice). The distance (d) between Ag and M increases in going from the first ($d \sim 4.6$ Å) to the fifth ($d \sim 11.4$ Å) neighbor configuration. It turns out that the configuration with Ag and Sb (or Ag and Bi) pair which are the second nearest neighbor of one another has the lowest energy. This means that Ag and Sb (or Ag and Bi) atoms like to come close to each other, bonded linearly through an intermediate Te, and form clusters or some sort

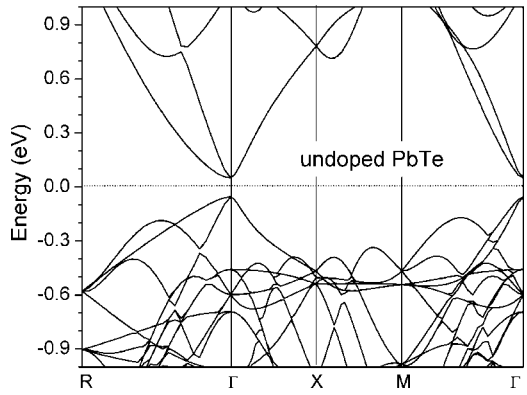

Figure 8. Band structure of undoped PbTe (64-atom supercell) along the high symmetry lines of the simple cubic Brillouin zone.

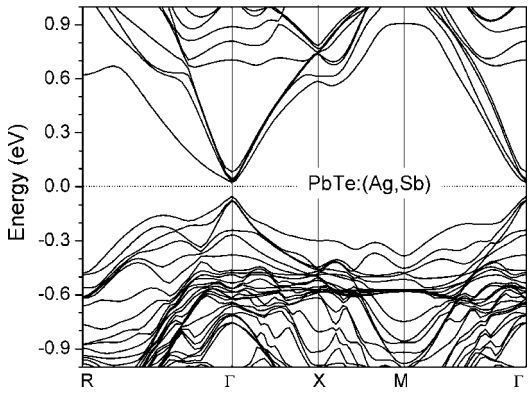

Figure 9. Band structure of PbTe doped with (Ag,Sb). Ag and Sb atoms in the pair are second-nearest neighbors to one another in a 64-atom supercell.

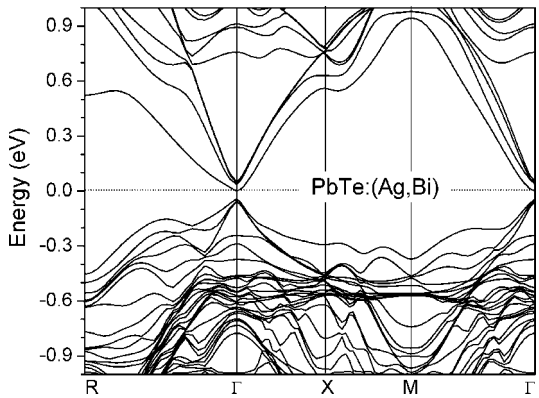

Figure 10. Band structure of PbTe doped with (Ag,Bi). Ag and Bi atoms in the pair are second-nearest neighbors to one another in a 64-atom supercell.

of embedded nanostructures.[40] We, therefore, have used this configuration for our electronic structure calculations.

In Figures 8, 9, and 10, we show the band structures of undoped PbTe and PbTe doped with (Ag, Sb) and (Ag, Bi), respectively, along the high symmetry directions of the simple cubic Brillouin zone (BZ).[41] There are band splittings coming from the presence of the (Ag,M) pairs because the symmetry is lowered compared to the undoped PbTe. The valence-band top is perturbed predominantly by Ag with an impurity-derived band formed predominantly out of Te p and Ag d states. This is the nearly flat band that forms the highest occupied band in Figure 9 or 10. This band is consistent with the resonant state near the valence-band top in the single-particle density of states (DOS) seen previously.[23] The conduction-band bottom is, on the other hand, perturbed predominantly by Sb (Figure 9) or Bi (Figure 10). There are splittings of the PbTe bands near the conduction-band bottom (predominantly Pb p bands) because of the presence of Sb (or Bi). The nearly flat bands seen in the energy range 0.6–1.0 eV above the Fermi level can be identified with the resonant states in DOS which are associated with Sb and Bi impurity atoms.[23] However, they affect the states near the bottom of the conduction band through hybridization effects quite differently. But, Ag plays a crucial role in determining the precise nature of the bands near the conduction band minimum (CBM). It helps push one of the bands (split off from the PbTe conduction band) down near the *R* point (of the simple cubic BZ) in going along the $\Gamma-R$ line (near ~0.6 eV). Detailed band structure analysis is presented elsewhere.[42]

The difference between Sb and Bi, which is important for transport, occurs near the Γ point. First, the band gap reduces from ~0.08 eV for (Ag, Sb) to ~0.04 eV for (Ag, Bi). Of course these band gap values are lower than expected which is a well-known LDA/GGA problem. However, the fact that Ag−Bi system has a smaller band gap than the Ag−Sb system should be true in an improved calculation. Second, in the case of the (Ag, Sb), a group of three nearly degenerate bands (we ignore the spin degeneracy) forms the lowest conduction band with a nondegenerate band (at ~0.06 eV above that group) at the Γ point (see Figure 9). In contrast, in the case of the (Ag, Bi) pair, the nondegenerate band forms the lowest conduction band and the group of three nearly degenerate bands is ~0.04 eV above the nondegenerate band at the Γ point (see Figure 10). Because of this basic difference in the arrangement of the bands and lower carrier concentration (*n*) in the Sb analog, one expects to see larger negative Seebeck coefficient in the Sb compounds compared to the Bi compounds, according to the expression for the thermopower for the degenerate semiconductor case,[43] eq 4:

$$S = \left(\frac{8\pi^{2/3}k_B^{\,2}(r+{}^3/_2)}{3^{5/3}eh^2}\right)\left(\frac{m^*}{n^{2/3}}\right)T \qquad (4)$$

where *r* is the scattering parameter. The effective mass *m** is inversely proportional to the mobility which is also affected by different scattering mechanisms. In addition to the above, because of the smaller band gap in the (Ag, Bi) system, intrinsic thermal excitations of electrons and holes will could further reduce the *n*-type Seebeck coefficient. These observations are consistent with our experimental findings.

Nanostructuring, Lattice Thermal Conductivity and

(40) Hazama, H.; Mizutani, U.; Asahi, R. *Phys. Rev. B* **2006**, *73* (11), 115108.
(41) Lax, M. *Symmetry Principles of Solid State and Molecular Physics*; 1974.
(42) Hoang, K. Atomic and Electronic Structure of Novel Ternary and Quaternary Narrow Band-Gap Semiconductors Ph.D. Thesis, Michigan State University: East Lansing, MI, 2007.
(43) Ravich, Y. I.; Efimova, B. A.; Smirov, I. A. *Semiconducting Lead Chalcogenides*; Plenum Press: New York, London, 1970, pp 155.

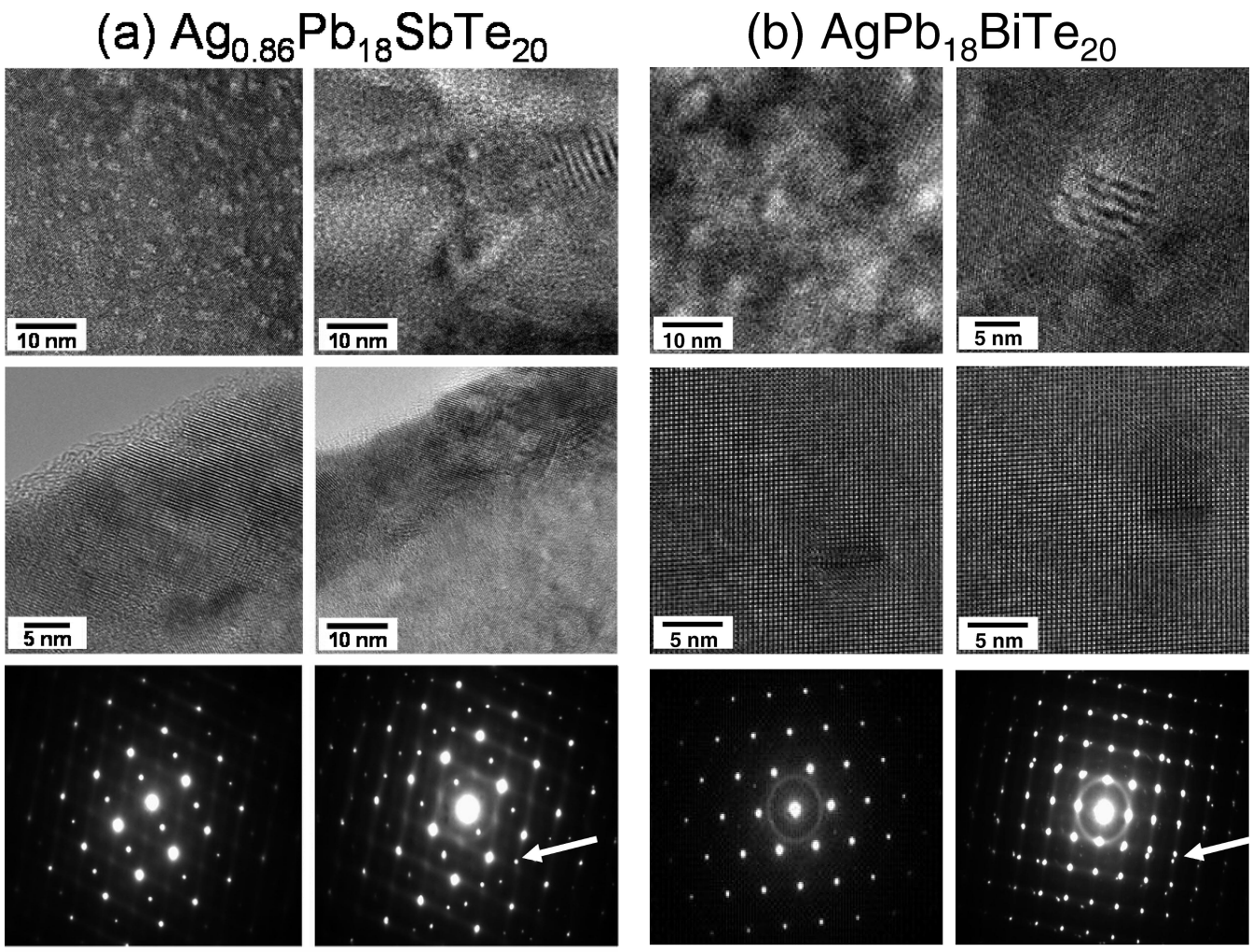

Figure 11. TEM images of (a) $Ag_{0.86}Pb_{18}SbTe_{20}$ and (b) $AgPb_{18}BiTe_{20}$.

Thermoelectric Figure of Merit. Previous studies involving transmission electron microscopy have shown that the LAST materials are heavily nanostructured with various kind of nanodots dispersed throughout a PbTe-rich matrix.[25,27] It is well-known that the presence of coherently embedded nanostructures in the bulk matrix is directly related to their enhanced thermoelectric performance, through reduced lattice thermal conductivity.[9,11] To investigate the influence of the substitution of Sb with Bi on the nanostructuring, samples were investigated under high resolution TEM (HRTEM). As shown in Figure 11 (middle), the HRTEM images of both samples indicate crystalline structure although the lattice fringes are not continuous and are broken by coherently embedded nanoparticles. Figure 11a shows that $Ag_{1-x}Pb_{18}SbTe_{20}$ ($x = 0.14$) contains local atomic ordering as well as nanostructuring associated with compositional fluctuations on the 2–5 nm scale. We observe crystal domain boundaries that are coherently grown. $Ag_{1-x}Pb_{18}BiTe_{20}$ ($x = 0$) system was also clearly nanostructured on 5–10 nm scale, shown in Figure 11b. From the low magnification TEM image of the sample (left top in Figure 11b), it shows the evenly dispersed nanoparticles. It also reveals the existence of lattice mismatch and possible fluctuations in composition. Selected area electron diffraction (SAED) measurements were performed on various areas, as shown in the diffraction patterns of Figure 11. The arrows in the diffraction patterns indicate the position of the extra diffracted intensity associated with nanostructuring.

The effect of these nanoscale inhomogeneities on the heat transport in these materials was studied with thermal diffusivity measurements as a function of temperature. Figure 12 shows the temperature dependence of the thermal conductivity of $AgPb_{18}BiTe_{20}$ sample. The total thermal conductivity

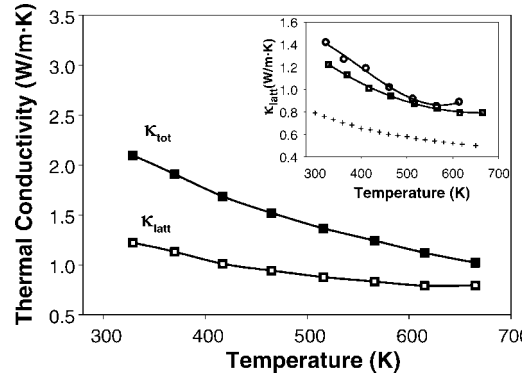

Figure 12. Temperature dependence of the total thermal conductivity (κ_{tot}, solid square) and lattice thermal conductivity (κ_{latt}, open square) of $AgPb_{18}BiTe_{20}$. The inset indicates the temperature dependence of the lattice thermal conductivity of $Ag_{1-x}Pb_{18}BiTe_{20}$ ($x = 0, 0.3$), compared with the lattice thermal conductivity (κ_{latt}) of $AgPb_{18}SbTe_{20}$ (presented as the + symbol).

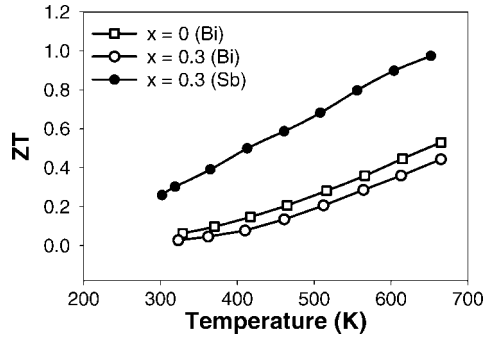

Figure 13. Temperature dependence of the dimensionless figure of merit ZT for $Ag_xPb_{18}BiTe_{20}$ ($x = 0$, 0.3) and $Ag_xPb_{18}SbTe_{20}$ ($x = 0.3$).

κ_{tot} was 2.2 W/m K at 320 K and decreased with increasing T. The total thermal conductivity (κ_{tot}) is the sum of two contributions, one from the charge carriers (κ_{elec}) and the other from the lattice vibrations (κ_{latt}), $\kappa_{tot} = \kappa_{elec} + \kappa_{latt}$.[44] Here, κ_{elec} is expressed by the Wiedemann–Franz law, $\kappa_{elec} = L_0\sigma T$, where L_0 is the Lorenz number and T is the absolute temperature. The value of Lorenz number for PbTe ($L_0 = 2.45 \times 10^{-8}$ W Ω/K^2)[45] is used to estimate κ_{elec}. The inset in Figure 12 shows the lattice thermal conductivity.

The κ_{latt} values of $AgPb_{18}BiTe_{20}$ and $Ag_{0.7}Pb_{18}BiTe_{20}$ at 300 K are ~1.2 and ~1.4 W/m·K, respectively. The κ_{latt} value of $AgPb_{18}BiTe_{20}$ corresponds to about a 50% reduction of the typical value of 2.3 W/m·K reported for PbTe. However, this value is larger than that of $AgPb_{18}SbTe_{20}$ (κ_{latt} value ~0.8 W/m·K at 300 K). This stronger scattering of phonons in the Sb containing materials is consistent with the previous result reported by Sootsman et al.[46] We attribute the different values of the lattice thermal conductivity for $AgPb_{18}BiTe_{20}$ and $AgPb_{18}SbTe_{20}$ to the differences in mass contrast of Bi and Sb with Pb, respectively. Because the mass difference between Pb and Bi is much smaller than that between Pb and Sb, for the same concentration, the resulting mass fluctuation scattering is stronger in the $AgPb_{18}SbTe_{20}$ system. Therefore, less phonon scattering exists in the Bi analogs leading to a higher lattice thermal conductivity.

Figure 13 shows the temperature dependences of ZT for the $Ag_{1-x}Pb_{18}BiTe_{20}$ ($x = 0$, 0.3) and $Ag_{1-x}Pb_{18}SbTe_{20}$ ($x = 0.3$). It can be seen that the value of ZT increases monotonically with an increase of temperature. The highest ZT values for $Ag_{1-x}Pb_{18}BiTe_{20}$ were 0.53 and 0.44 for $x = 0$ and $x = 0.3$ at 665 K, respectively, compared to those of the $Ag_{1-x}Pb_{18}SbTe_{20}$ ($x = 0.3$) samples of ZT ~ 1.0 at 650 K. The considerably lower ZT observed for $AgPb_{18}BiTe_{20}$ is attributed mainly to the small values of Seebeck coefficient and the higher lattice thermal conductivity.

Concluding Remarks. The synthesis of $Ag_{1-x}Pb_{18}BiTe_{20}$ with an average NaCl-type structure was accomplished. These materials were studied comparatively with the antimony analogs LAST-18. For the same compositions for both systems, the electrical conductivity is nearly comparable while the Seebeck coefficient decreases dramatically by substituting Sb with Bi. The larger Seebeck coefficient of $AgPb_{18}SbTe_{20}$ may be attributed partly to the lower carrier concentration and higher mobilities than in the Bi analogs. Also there are fundamental differences in the electronic structure of Sb and Bi analogs near the band gap region. These may be responsible for the observed differences in transport properties of LAST-18 and BLST-18 systems. Despite the presence of significant nanostructuring, the reduction in the lattice thermal conductivity observed for the Bi analog is not as strong as in the Sb systems. This could be attributed mainly to the diminished atomic mass contrast between the nanostructures and the matrix in the $AgPb_{18}BiTe_{20}$ system although this conclusion must be tentative since the extent of nanostructuring may not be the same in both systems.

Finally, under the same preparation conditions and composition the Bi analogs contain more carriers and consequently, have lower thermoelectric power. Therefore, the higher lattice thermal conductivity, together with the lower Seebeck coefficient result in lower ZT for $Ag_{1-x}Pb_{18}BiTe_{20}$. A higher ZT may be achieved in this system if the carrier concentration could be decreased through proper doping or change in composition. This will be explored in future experiments. It is apparent for now that the identity of the trivalent element is essential in obtaining enhanced thermoelectric properties in PbTe derived materials. In the $Ag_{1-x}Pb_{18}MTe_{20}$ (M = Sb, Bi) systems, Sb is more effective in improving the thermoelectric performance of PbTe-based systems than Bi. This is consistent with previous results on the thermoelectric performance of PbTe nanostructured with Sb vis-à-vis Bi nanoparticles.[46]

Acknowledgment. This work was supported by the MURI Grant No. N00014-03-10789 from the Office of Naval Research and the (MURI program).

CM703661G

(44) DiSalvo, F. J. *Science* **1999**, *285*, 703.
(45) Orihashi, M.; Noda, Y.; Kaibe, H. T.; Pantsulaya, I. A.; Varlamov, A. A. *Phys. Rev. B* **1994**, *245*, 160.
(46) Sootsman, J. R.; Pcionek, R. J.; Kong, H.; Uher, C.; Kanatzidis, M. G. *Chem. Mater.* **2006**, *18*, 4993.